

Relationship Between Sea Surface Temperature Anomalies In The Southwestern Atlantic Continental Shelf And Atmospheric Variability On Intraseasonal Timescales

Moira Luz Clara (✉ mluzclara@inidep.edu.ar)

INIDEP: Instituto Nacional de Investigacion y Desarrollo Pesquero <https://orcid.org/0000-0002-7539-5292>

Mariano S. Alvarez

CIMA: Centro de Investigaciones del Mar y la Atmosfera

Carolina Vera

CIMA: Centro de Investigaciones del Mar y la Atmosfera

Claudia G. Simionato

CIMA: Centro de Investigaciones del Mar y la Atmosfera

Andrés J. Jaureguizar

CIC: Comision de Investigaciones Cientificas de la Provincia de Buenos Aires

Research Article

Keywords: Sea surface temperature, Intraseasonal variability, Austral warm season, Ocean-Atmosphere teleconnections

Posted Date: July 8th, 2021

DOI: <https://doi.org/10.21203/rs.3.rs-588846/v1>

License: © ⓘ This work is licensed under a Creative Commons Attribution 4.0 International License.

[Read Full License](#)

Abstract

The intraseasonal (IS) variability of the sea surface temperature (SST) in the Southwestern Atlantic Northern Argentinean Continental Shelf (SWACS NACS, 45-33°S - 70-50°W), and its relationship with that in the atmosphere, was studied for the austral warm season. SST satellite data (11-km resolution NOAA CoastWatch Program) and data of different atmospheric variables (Reanalysis1 NCEP/NCAR and ERA-Interim) were used. Data were filtered using a 10-90day filter to isolate the IS variability. A Principal Component analysis was applied then to the filtered SST anomalies (SSTA) and the activity of the leading modes was described through the corresponding temporal series. The first three modes are significant. EOF1 (25.7% of variance) exhibits SSTA of opposite sign to the north/south of 42°S. EOF2 (9.0%) and EOF3 (5.1%) are related with centers of SSTA of opposite sign located off the Uruguayan coast and in the middle shelf. Composites of SSTA and of key atmospheric variables were made considering the days in which the main modes were active. They show that the SSTA described by the three modes are associated with distinctive regional sea level pressure anomalies that, in turn, seem to be related to atmospheric Rossby wave trains extending from the Australia area towards South America. The corresponding atmospheric wave sources vary depending on the mode. These results show, therefore, that the SSTA in the SWACS NACS exhibit significant IS variability that is, in part, locally and remotely influenced by atmospheric anomalies oscillating on similar timescales. These ocean-atmosphere teleconnections could help to improve ocean predictability at those timescales in the future.

Introduction

Profound knowledge of sea surface temperature (SST) anomalies distribution over the continental shelves is essential to study oceanic processes such as frontal dynamics, upwelling and downwelling events, as well as eddies and plumes evolutions, which are also important in biological applications. The knowledge of SST anomalies in the shelves is also useful for climate monitoring and prediction, since they respond to a multiple-scale organization of atmospheric circulation anomalies occurring over distant parts of the globe, commonly called teleconnections. Climate teleconnections can exhibit variability on intraseasonal (IS) time scales, which are those between 10 and 100 days (Feldstein, 2003; Murakami, 1981; Wang *et al.*, 2016). Moreover, in recent years there has been a greater appreciation of the importance of the two-way interactions between the tropics and the mid-latitudes and high latitudes on IS time scales (Stan *et al.*, 2017). Whereas mid-latitudes are typically characterized by being energetic areas where eastward-moving atmospheric baroclinic waves dominate surface energy flux variations on synoptic timescales (3 to 10 days), quasi-stationary large-scale Rossby waves, blocking anticyclones as well as slowly moving cutoff lows contribute significantly to extratropical atmospheric variability on timescales longer than approximately 10 days (Alexander and Scott, 1997; Deser *et al.*, 2010). Berbery and Nogués-Paegle (1993), among other early studies, showed that austral summer atmospheric convection variability over the Indonesia region contributes to induce atmospheric Rossby wave trains that propagate poleward from this region towards South America and the Southwestern Atlantic Ocean (SWAO). More recently, the description and understanding of the atmospheric IS variability between 10

and 90 days has received considerable attention at both global and regional scales. Results show that atmospheric IS variability is essentially internally generated by atmospheric instability (Stan *et al.*, 2017). The Madden-Julian Oscillation (MJO) is recognized as the leading global pattern on IS timescales, with maximum amplitude at the tropics and dominant activity between 30 and 60 days (*e.g.*, Madden and Julian, 1972). The MJO is characterized by a wavenumber 1 spatial structure propagating eastwards influencing not only atmospheric variables such as air temperature, pressure, winds, cloudiness and rainfall, but also ocean conditions like SST, ocean surface evaporation, and ocean chlorophyll (Madden and Julian, 1972; Hendon and Salby, 1994; Zhang, 2005).

The IS atmospheric variability over South America and the surrounding oceans has received some attention from the scientific community during the last twenty years. Vera *et al.* (2017), and references therein, show that it exhibits considerable amplitude all year round, with large and significant influence on regional climate conditions. The South Atlantic Convergence Zone (SACZ), which is a band of active atmospheric convection that develops during the warm season (Carvalho *et al.*, 2004), plays a key role in determining the leading patterns of regional atmospheric IS variability (*e.g.*, Vera *et al.*, 2017). Based on observations and reanalysis (Alvarez *et al.*, 2016, 2017) and numerical models (Barreiro *et al.*, 2018) it has also been confirmed that the regional IS atmospheric variability is in part influenced by the MJO activity, where the Atlantic air-sea interaction was found to be important to enhance the rainfall within the SACZ through a local warm SST anomaly forced by heat flux anomalies associated with the direct MJO impact. Air-sea interaction over the SACZ region can be directed from ocean to atmosphere, from the atmosphere to the ocean, be mutual or neutral, and each interaction is associated with distinct atmospheric anomalies (Tirabassi *et al.*, 2014).

The study of SST variability in the Southwestern Atlantic has received considerable attention on annual (*e.g.*, Podestá *et al.*, 1991; Lentini *et al.*, 2000; Rivas, 2010; Simionato *et al.*, 2010; Delgado *et al.*, 2014; Luz Clara *et al.*, 2019), interannual and decadal timescales (*e.g.*, Venegas *et al.*, 1997; Paegle and Mo, 2002; Sterl and Hazeleger, 2003). Performing numerical experiments with both atmospheric and ocean global models, Rodrigues Chaves and Nobre (2004) showed the predominance of a negative thermodynamic feedback between the atmosphere and the ocean over the southwest tropical Atlantic during strong SACZ events. They conclude that negative SST anomalies often observed underlying the SACZ represent an oceanic response to atmospheric forcing.

The surface ocean conditions in the Southwestern Atlantic Northern Argentinean Continental Shelf (SWACS NACS) present a very marked SST annual cycle, explaining over 90% of the total variance (Luz Clara *et al.*, 2019). It is characterized by SST amplitude diminishing offshore and southward, and with maximum amplitudes in the inner Río de la Plata and El Rincón areas (Podestá *et al.*, 1991; Rivas, 2010; Simionato *et al.*, 2010; Delgado *et al.*, 2014; Luz Clara *et al.*, 2019). Regarding the SST variability on shorter time scales (synoptic to intra-seasonal), it is known that the wind variability has a large impact on coastal dynamics (Guerrero *et al.*, 1997; Framiñan, 2005; Pimenta *et al.*, 2008; Simionato *et al.*, 2006, 2007, 2010; Saraceno *et al.*, 2014). Dominant winds, that vary from the northeast to the southwest in a scale of a few days (Simionato *et al.*, 2005, 2007), produce alternating events of downwelling and

upwelling that cool and heat surface waters along the Uruguayan coast (*e.g.*, Framiñan, 2005; Pimenta *et al.*, 2008; Simionato *et al.*, 2010; Trinchin *et al.*, 2019). In addition, other atmosphere-ocean interaction processes such as marine heat waves have been lately studied in the SWACS. Marine heat waves in the Atlantic ocean are caused by persistent anticyclonic circulation associated with atmospheric blocking, which is in turned triggered by tropical convection in the Indian and Pacific oceans (Rodrigues *et al.*, 2019), probably associated with the MJO (Manta *et al.*, 2018), being this mode of variability a key source of long-term variability in subtropical South America blocking frequency (Rodrigues and Woollings, 2017).

However, SST variability on IS timescales on the SWACS NACS and its relationship with atmospheric circulation anomalous patterns have not been fully studied yet.

The aim of this paper is, therefore, to describe the IS variability of the SST anomalies in the SWACS NACS and to explore the associated atmosphere-ocean interaction mechanisms. The study focuses particularly on the warm season, that is when regional atmospheric IS variability is strong in association with the SACZ activity (Vera *et al.*, 2017) and when IS variability of SST in the SWACS presents higher activity, as will be shown below.

Data And Methods

SST daily data used for this study (hereafter also referred to as satellite data) is a satellite product obtained from the NOAA CoastWatch Program. Data are mapped into a regular grid of $0.1^\circ \times 0.1^\circ$, and available on daily composites derived from 5-day running averages for the period extending from July 2002 to March 2014.

SST data were estimated by optimal interpolation methods merging SST observations coming from infrared and microwave sensors installed on multiple platforms. These merged, or “blended”, products have good spatial coverage and a low total error compared with the individual errors for each instrument. Reynolds *et al.* (2002) showed that those errors can be dramatically reduced in infrared-microwave sensors combinations. In areas where data are scarce, such as the SWACS NACS region, those blended products provide an opportunity of evaluating SST variability even on relatively short time scales (Simionato *et al.*, 2010). The data processing is described in Powell *et al.* (2008).

The seasonal cycle was calculated from the SST data, first adjusting minimum squares sinusoidal functions (harmonic analysis) to the raw daily observations (linear-trend-removed) at every grid point, and then computing the combination of the corresponding annual and semiannual oscillations. The residues after removing the seasonal cycle from the raw data are regarded as the temporal anomalies that describe the transient variability. The inter-annual anomalies were determined by simply subtracting the annual means from the seasonal cycle. The signals obtained after subtracting both seasonal and inter-annual anomalies from the raw data were considered as the SST anomalies (SSTA) on sub-annual time scales. SSTA were then filtered to retain only IS variations using a 10–90-day bandpass Lanczos filter with 101 weights (Duchon, 1979). An Empirical Orthogonal Functions (EOF) analysis was then performed

to identify the leading patterns of SSTA variability over the SWACS NACS region. In this case, the S-mode covariance matrix of SSTA was used as input for the EOF analysis. A Fisher test was implemented to evaluate the statistical significance of the variances using a confidence level of 95 %.

The associated dynamic processes were explored by computing daily mean composites (averages) of the 10-90-day bandpass Lanczos filtered anomalies of different variables taken from the ERA Interim database (Dee *et al.*, 2011): SST, 925-hPa air temperature, sea level pressure (SLP), wind at 10m and geopotential height (GPH) at 300 hPa. Anomalies were obtained for every variable by first removing the linear trend and then the first three harmonics of the daily average of the period 1979–2016. Daily stream function (STR) at 250 mb derived from NCEP/NCAR reanalysis dataset (Kalnay *et al.*, 1996), were also considered for the period 1999–2018. Anomalies were computed following the same method as for the GPH though using the available reference period.

Composite significance was tested using a Monte Carlo approach by resampling events to perform the composites: the day and year of the beginning of each event was randomized 10 thousand times preserving the length of each event, and these random composites were computed to build a random distribution. In this way, the persistence of anomalies is taken into account. The 2.5 and 97.5 percentiles were used to consider the 5% significant values for each variable and grid point.

Results

3.1. Leading patterns of SST IS variability

Variability on the intra-seasonal time scale accounted for up to 50% of the total SSTA variance. Highest values of IS variance were observed over the Río de la Plata Estuary (RDP; **Fig. 1**), in the middle continental shelf north of 40°S, and in coastal areas, particularly along the coast of El Rincón (ER; **Fig. 1**) area. Instead, minimum values were observed south of 40°S in the outer shelf.

The EOF analysis applied to the daily filtered SSTA indicated that nearly 40% of the variance is explained by the first three EOFs (**Fig. 2**); they accounted for 25.7%, 9.0% and 5.1% of the variance, respectively.

The leading pattern, EOF1 (**Fig. 2.a**), exhibited scores of opposite signs north and south of 40°S, approximately, though the magnitude is greater in the north; it showed high activity all year round (**Figs. 3.a, 3.b**). The second leading pattern, EOF2 (**Fig. 2.b**), showed scores of opposite signs between the southern Uruguayan coast (Punta del Este region, PDE; **Fig. 1**) and the rest of the continental shelf, with maximum negative values north of Middle Shelf Front (MSF; the area spanning between 38°S and 42°S between the 30 m and 80 m isobaths). The third leading pattern, EOF3 (**Fig. 2.c**), exhibited three principal centers of action of alternating signs located at PDE (positive), at the middle shelf out of the RDP (negative) and on the MSF region extending to the coast (positive).

The temporal evolution of the three leading patterns was analyzed to better understand their characteristics. A positive (negative) event of any of the three patterns was defined as the sequence of

more than three consecutive days associated with loading values above 0.4 (below -0.4), thresholds that correspond to the mean value of the positive (negative) loadings plus (minus) one standard deviation. A summary of the positive and negative events identified for the three leading patterns is presented in **Table 1**. Events are described separately for the warm (ONDJFMA) and the cold (MJJAS) austral seasons of the year. The seasonal separation is motivated by the fact that atmospheric circulation anomalies exhibit on IS timescales distinctive features associated with the presence of the SACZ during the warm season or with its absence in the cold season (Vera *et al.*, 2017). **Table 1** also includes the dates of occurrence of the shortest and longest events identified. The summary shows that around 60% of total EOF1 events (warm and cold seasons) were negative; for the cold season, 75% of EOF1 events were negative, while for the warm season, 53% of those events were negative. Whereas the number of positive and negative EOF1 events was similar during the warm season, the negative ones dominated during the cold months with an average duration of 4 days for the shortest events and 11 days for the longest. Most of the events for both EOF2 and EOF3 occurred during the warm period, with an average duration of 26 and approximately 13 days for the largest events, respectively. Therefore, as (i) the warm season shows the largest activity of these IS modes of variability, that (ii) it is when regional atmospheric IS variability is intense due to the SACZ activity (Vera *et al.*, 2017), and (iii) the ocean-atmosphere interaction has been detected in summer (Rodrigues Chaves and Nobre, 2004), in what follows we focus our analysis on the warm season. For the interested reader, the time series of the principal components (PC or loadings) associated to the first 3 SST EOFs are presented in the supplementary Fig. 1, for the ONDJFMA season.

3.2. Composites of high-resolution SST anomalies

Composites of the SSTA from satellite data (**Fig. 3**) were computed considering the positive and negative events identified during the warm season. EOF1 positive events were associated with SST negative anomalies over the entire shelf north of 41°S , with values cooler than -1°C in and around the RDP and the Uruguayan coast (**Fig. 3.a**). Instead, EOF1 negative events were related to positive SSTA in most of the northern shelf, maximizing in and around the RDP (**Fig. 3.b**). The composite for EOF2 positive events exhibited positive SSTA over 0.3°C along the PDE region northern portion of the RdP (**Fig. 3.c**), maximizing in the, and around Península Valdés (PV; **Fig. 1**). SSTA composite for negative EOF2 events displayed strong positive anomalies (over 0.5°C) in the MSF area, with a strong center ($> 1^{\circ}\text{C}$) in the northern shelf area, centered at 37°S (**Fig. 3.d**), and negative anomalies centered in PDE area. SSTA composite for EOF3 positive events (**Fig. 3.e**) showed low significant SSTA values ($\sim 0.3^{\circ}\text{C}$), positive anomalies in PDE MSF area and negative ones around 36.57°S and south of 42°S . The negative phase of EOF3 was characterized by an SSTA composite field with negative anomalies ($\sim 0.4^{\circ}\text{C}$), with low significance, over the MSF region, between 38°S and 42°S , and around PDE, and low positive values anomalies (~ 0.73) south of 42°S , maximizing close to the coast (**Fig. 3.f**).

Table 1. Summary of significant events identified for the three SSTA leading patterns: EOF1, EOF2 and EOF3. Positive (negative) events were defined as the sequence of more than three consecutive days associated with loading values > 0.4 (< -0.4). Events are described separately for the warm (ONDJFMA) and the cold (MJJAS) austral seasons of the year.

	TOTAL		Warm austral season (ONDJFMA)		Cold austral season (MJJAS)	
	# POSITIVE events	# NEGATIVE events	# POSITIVE events	# NEGATIVE events	# POSITIVE events	# NEGATIVE events
EOF 1	17	27	13	15	4	12
Shortest event date - length			Nov'02 Mar'08 Dec'08 Apr'12 Apr'13 4 days	Nov'11 3 days	Jul'05 4 days	Jul '10 3 days
Largest event date - length			Feb'05 8 days	Nov '08 11 days	Sep'05 8 days	Sep'07 12 days
EOF 2	28	30	25	28	3	2
Shortest event date - length			Nov'12 4 days	Dec'04 Jan'05 Oct'07 Jan'10 Apr'11 3 days	Aug'09 3 days	May'04 3 days
Largest event date - length			Jan'13 31 days	Feb'13 21 days	Aug'02 Sep'07 7 days	Sep'07 6 days
EOF 3	33	30	27	26	6	4
Shortest event date - length			Feb'04 Dec'04 3 days	Apr'05 Apr'09 Mar'10 Sep'11 Apr'12 3 days	Aug'02 Sep'03 3 days	Jun'09 Jul'12 4 days
Largest event date - length			Oct'04 12 days	Dec'02'10 15 days	Jul'12 6 days	May'07 6 days

3.3. Dynamics

Composites for different variables were also computed based on the positive and negative events identified for the three leading EOFs during the warm season. Focus is made in exploring the physical mechanisms associated with the air-sea interaction. For each EOF, composites are described first on a regional domain and then over a large-scale domain to assess the role of atmospheric variability in explaining the regional atmospheric circulation anomalies. The latter was motivated by previous results (*e.g.*, Vera *et al.*, 2017, and references therein) showing the significant influence of tropical atmospheric convection variability as well as of the atmospheric jet stream instabilities, on regional atmospheric circulation anomalies on IS timescales.

3.3.1. EOF1

Composites of SSTA from ERA-Interim datasets for EOF1 positive events (**Fig. 4.a**) show negative values dominating over the SWAO between 30°S and 44°S and further north along the Brazilian coast. Positive SLP anomalies dominate the oceanic region, with its center over the Malvinas Islands and maximum values zonally extended at around 55°S, as well as over Argentina (**Fig. 4.c**). In agreement, northwestward wind anomalies are observed off the coast of central Argentina, which favor cold advection and the retreat of the Brazil current to the north. The latter is also seen by the northward wind anomalies eastward of the Brazilian coast (**Fig. 4.b**), and therefore explaining the SST pattern. Composites for air temperature anomalies at 925 hPa for EOF1 positive events are positive over south Argentina and negative over the northeastern region of Argentina, including the RDP area and the continental shelf north of 30° S. The cold air-temperature anomalies might influence the SST anomalies of the RDP estuary, as its temperatures are usually warmer than those of the continental shelf during summer. But in this case, the water might be losing heat to the atmosphere through sensible heat fluxes. Composites for STR anomalies over the large-scale domain (**Fig. 7.a**) confirm that the anticyclonic anomaly observed over the southwestern Atlantic is embedded in a Rossby wave train extended along an arch from Australia

towards the southeastern Pacific and then South America. The wave activity fluxes show that energy is propagated along this wave train, suggesting that the regional anomalies are remotely influenced by tropical variability (**Fig. 7.a**). This wave train is the most prominent feature of the southern hemisphere circulation as seen in the 300 mb IS-filtered geopotential height anomalies composites (**Fig. 8.a**).

Composites for the EOF1 negative events show that positive SSTA prevail in the SWACS southwestern Atlantic region north of 44°S (**Fig. 4.d**). Negative SLP anomalies are large and zonal at middle latitudes, centered around 55°S (**Fig. 4.f**) and favoring southward wind anomalies at low levels along the coast of Brazil. Therefore, in contrast to the composites for EOF1 positive events, warm waters of the Brazil current can extend farther south explaining the positive SST anomalies observed for EOF1 negative events. Moreover, the corresponding air temperature composites show positive anomalies over eastern Argentina and the Atlantic Ocean north of 45° S, which may also favor downward sensible heat fluxes and warmer-than-normal SSTs over the whole area (**Fig. 4.h**).

In these negative EOF1 events, the Rossby wave train in which the upper-level cyclonic STR anomaly over the southern tip of South America is embedded, seems to extend more from the west than for EOF1 positive events (**Fig. 7.b**), and it refracts with a stronger meridional component over South America. Composites for GPH anomalies in polar stereographic projection (**Fig. 8.b**) show that the cyclonic anomaly extended along the southern tip of South America seems to be associated with a zonally symmetric pattern of upper-level atmospheric circulation anomalies, in which cyclonic anomalies dominate at middle latitudes and anticyclonic ones at higher latitudes, resembling a negative phase of the Southern Annular Mode (**Fig. 8.b**). Moreover, when computing the average of the SAM index for each negative event, it is found that more EOF1 events occur in association with negative SAM index values (not shown). Accordingly, previous studies (e.g., Carvalho *et al.*, 2015; Pohl *et al.*, 2010; Flatau and Kim, 2013) show evidence of SAM activity on circulation anomalies in the Southern Hemisphere on IS timescales.

3.3.2. EOF2

The composites of SSTA from ERA Interim dataset for positive EOF2 events show large negative anomalies with maximum magnitudes over the SWACS NACS (**Fig. 5.a**). A negative SLP anomaly is centered at around 35°W 45°S, which is mainly related to with northeastward wind anomalies off the coast of Uruguay, forcing the retreat of the Brazil current to the north. Negative air temperature anomalies for positive EOF2 events are on average observed farther away from the coast directly related to the location of the SLP anomalies more to the east. The patterns for positive EOF2 events can be explained in terms of cold air temperature and wind forcing over the shelf: according to the barotropic vorticity balance in the ocean, the circulation gets the sign of the wind stress curl; in this case this would produce advection of cold waters from the south to the north, cooling the area. Note also that the atmosphere is cold over the region; this could favor the loss of sensible heat by the ocean, contributing to the observed cooling as well (**Fig. 5.g**). At the large-scale, composites of STR anomalies (**Fig. 7.c**) show weak activity over the South Pacific Ocean, and the hemispheric perspective of GPH anomalies (**Fig. 8.c**) reveals that the cyclonic circulation anomaly observed over the southwestern Atlantic is part of a planetary

wavenumber-4 structure extending along the middle latitudes in the Southern Hemisphere but that is more defined over the Southern Atlantic and the Indian Ocean regions.

For negative EOF2 events, positive SSTA (ERA-Interim) prevail in the southwestern Atlantic, with larger values between 35 and 45°S (**Fig. 5.d**). Negative SLP anomalies extend over the southeastern Pacific and the continent's southern tip, while a center of positive SLP is located eastward centered in 45°S-30°W (**Fig. 5.f**). In agreement, wind anomalies describe a large anticyclonic circulation, with a southwestward component and larger magnitude at the subtropics and southward further south (**Fig. 5.e**). The anticyclonic atmospheric circulation would lead in the ocean an anomalous anticyclonic circulation along the coast (southward), driving warm waters and giving rise to the generalized warm SSTA pattern observed. In this case the atmosphere is warmer over the region; this could reduce the loss of sensible heat by the ocean, contributing to the observed warming as well (**Fig. 5.h**). In turn, the northeast wind anomaly over the RDP will produce a retraction of the freshwater plume to the southeast and an increase in upwelling producing the cold signal that is seen along the coast of the RDP that is seen in the composites of the satellite data (**Fig. 3.d**).

Figure 8.d shows that the regional atmospheric circulation anomalies are in upper levels associated with a wavenumber-4 structure at middle latitudes for the negative EOF2 cases, and as in the positive EOF2 cases, more intense over the south Atlantic and Indian Oceans. Therefore, EOF2 seems to be related to the wavenumber 4 that, according to its phase, favors a positive or a negative EOF2 event.

3.3.3. EOF3

EOF3 positive events are associated with negative SSTA (as described by ERA-Interim dataset) in regions of the Argentinean coast between 36° S and 38°S and around 45°S, (**Fig. 6.a**). Moreover, a center of negative SLP anomaly values is centered in the SWAO (**Fig. 6.c**) which promotes south of 40°S large northward wind anomalies along the coast, and northeastward anomalies at that latitude (**Fig. 6.b**). These wind anomalies along with the cold air temperature anomalies in low levels (**Fig. 6.g**) may be forcing cold SSTA over the mentioned areas through advection and loss of sensible heat to the atmosphere.

The regional circulation anomaly is, in upper levels, part of a coherent Rossby wave train emanating from northwestern Australia, with a strong positive anomaly west of the Antarctic Peninsula and a cyclonic anomaly downstream over in the Atlantic Ocean. Furthermore, anticyclonic anomalies, though weak, are observed over Antarctica, which might be associated with a SAM negative phase (**Fig. 8.e**). It was also found that most of EOF3 positive events are related to negative SAM index values (not shown).

EOF3 negative events are associated with positive ERA-Interim SSTA dominating further south of 44° S and around 38°S (**Fig. 6.d**). A large and intense center of positive SLP anomalies is located at around 45°W, 50°S (**Fig. 6.f**), which is associated with strong southwestward wind anomalies (**Fig. 6.e**). As for the positive EOF3 events, advection of warmer waters to this region might explain the SSTA, as well as

sensible heat fluxes from the atmosphere to the ocean in association with the warm air temperature anomalies (**Fig. 6.h**).

The upper-level atmospheric circulation related to the EOF3 negative events (**Fig. 7.f**) shows a Rossby wave train emanating from western Australia in opposite phase than in the positive EOF3 cases, with a cyclonic anomaly west of the Antarctic Peninsula and a strong anticyclonic anomaly downstream over the southwestern Atlantic Ocean. This pattern is also clear in the GPH anomalies in **Fig. 8.f**, and, on average, SAM phases during these events are positive (not shown).

Conclusions

This work examines the main features of SST variability in the SWACS NACS in the intraseasonal time scale and assesses the relationship of this local variability with that observed in the SWAO and the Southern Hemisphere. Results are based on EOF analysis of IS-filtered SST daily anomalies, where three main patterns were obtained, and compositions of oceanic and atmospheric variables were made considering the days in which those modes were active.

For positive (negative) phases of EOF1, SSTA composites in the SWAO showed negative (positive) values along the eastern coast of southern South America to the north of 41°S, with more intensity in the RDP area. The wind composite anomaly for EOF1 showed southeast anomaly directions with variable intensities over the Argentinean coast for the positive cases and intense anomaly from the west/northwest directions all over the SWACS NACS. Composites for SLP anomalies corresponding to this mode showed the largest magnitude along the 50°S latitude, with maximum SLP anomalies extend to the east of the continent associated with the positive phase, and negative SLP anomalies associated with the negative phase extended from the southeastern Pacific eastward into the Atlantic. The wind and SLP patterns obtained for EOF1 positive mode should have shown an SSTA different from that shown in **Fig. 3.a**, since an anticyclonic anomaly of the atmospheric circulation would induce an oceanic circulation coming from the south, which, in summer, would transport the warm water from the estuary northwards on the continental shelf. Therefore, the great cooling of the atmosphere observed over the region (**Fig. 4.g**, air temperature) might be causing the cold SSTA observed throughout the RDP. Upper-level stream function anomalies show the presence of a corresponding large-scale pattern of alternating positive and negative circulation anomalies, coming from western tropical South Pacific. Those alternating anomalies are evidence of atmospheric Rossby wave trains that can either be excited by instabilities in the midlatitudes westerly jets or by the atmospheric tropical convection. In particular, the anticyclonic anomaly observed over the southwestern Atlantic in the EOF1 positive phase is associated with a planetary wavenumber 3 structure extended at around the 50°S in superposition with a Rossby wave train extended along an arch from Australia towards southern South America. On the other hand, the EOF1 negative phase shows that the cyclonic anomaly extended along the southern tip of South America is associated with a more zonally symmetric pattern of upper-level atmospheric geopotential height anomalies being cyclonic at middle latitudes and anticyclonic at higher latitudes, resembling a negative phase of the SAM Southern Annular Mode (**Fig. 8.b**).

EOF2 composites exhibit statistically significant SSTA around RDP and PDE for both modes. The composite for the negative EOF2 events displays an over 0.5°C positive SSTA in the MSF area north of 41° S. These anomalies can be explained in terms of the wind force over the SWAO. Since the oceanic circulation in the region is dominated by the wind curl, its sign is the sign of the wind curl. For the negative case, ocean circulation will be anticyclonic and southward along the coast since wind anomalies exhibit a large anticyclonic circulation (**Fig. 5.e**). This circulation would drive warm water to the south bringing a warm SSTA pattern. Stream function anomalies (**Fig. 7.d**) showed that regional wind anomalies are part of a Rossby wave train coming from the Indian/Pacific Ocean. This mode could also be associated with upwelling events at the Uruguayan coast, though it may not be appreciated in this data set because of the spatial resolution. However, in a recent study performed with more accurate satellite data resolution this upwelling is revealed (Trinchin *et al.*, 2019).

SSTA composites for positive EOF3 events showed significant values in outer MSF, with positive anomalies, and the RDP mouth southernmost area, with negative anomalies. In the case of negative events, SSTA composites showed anomalies around - 0.5°C over the MSF area between 38 and 42° S, and very low positive anomalies between 36 and 38 °S (**Fig. 3.f**).

There are different processes related to atmospheric forcing that could be involved with SST variability at different time scales. Kara *et al.* (2009) showed, from climatological monthly global means, that SST variations at all latitudes are generally strongly and positively correlated with increases in near-surface air temperature, and with vapor mixing ratio and net shortwave radiation at the sea surface, although they are often moderately and negatively correlated with increases in near-surface wind speed. Particularly, variations in the net shortwave radiation and vapor mixing ratio are found to have more influence in driving the seasonal cycle of SST than other atmospheric variables. A study of the variability of the SWAO shelf circulation based on a high-resolution ocean model, revealed that there is an abrupt change of the dynamical characteristics of the circulation at 40° S (Combes and Matano, 2018). South of that latitude, the seasonality is driven by onshelf fluxes coming from austral currents, and interannual variability of the shelf circulation is principally wind-driven. North of 40° S, the local wind forcing drives the seasonal variations of the shelf transport, while the interannual variability of the flow is driven by RDP runoff combined with local wind stress and the Brazil-Malvinas confluence (Combes and Matano, 2018). Over the SWACS, SAM-induced along-shore wind stress anomalies modulate the along-shore transport variability. This mechanism holds also at synoptic scales, highlighting the dominant role of the wind on the along-shore transport (Lago *et al.*, 2021). Scasso and Piola (1998) showed that there is an exchange of net heat between the continental shelf water and the atmosphere through latent heat flux, resulting in excess evaporation (E) over precipitation (P). While flowing towards lower latitudes, the water experiences an increase in salinity along its path over MSF area and, as the process of evaporation will absorb heat from the surrounding waters, a cooling of SST. The net air-sea exchange of water in the SMG area shows similar seasonality as the E rate (i.e., with a minimum in austral spring and a maximum in the fall (Scasso and Piola, 1988)) while the P rate is nearly constant throughout the year. On the other hand, Luz Clara *et al.* (2019) identified the presence of a warm water mass in the same region (where E > P) in the transition seasons: minimum E rates in austral spring suggest less ocean heat loss, and thus, warmer

SSTs; whereas in the fall, the SMG water begins to cover the ER area and the excess of E is at its peak, thus, the loss of heat through latent heat flux is greater, resulting in cooler SSTs. This exchange of net heat mechanism could be involved in the SST variability observed in the results of the present work. We believe the present study is the starting point to a profound budget analysis in the future.

Throughout this work, we showed that the SST anomalies in the SWACS NACS exhibit significant IS variability that is, partially, influenced by that in the atmosphere on similar timescales, not only on the ocean in mid-latitudes but also extended in the tropical zones of the Pacific and South Indian Oceans. These ocean-atmosphere teleconnections could help in the future to improve ocean predictability at those timescales, particularly in the SWACS NACS, where ecosystems are highly productive and diverse, with socio-economic relevance for Argentina, Uruguay and Brazil, and have a complex oceanographic dynamic (Lercari *et al.*, 2019). For example, the demersal fish distribution is mainly associated with environmental gradients along the SWACS NACS, where temperature and salinity are environmental parameters that have physiological importance and have a direct influence on fish distribution at all spatial scales (*e.g.*, Jaureguizar *et al.*, 2006, 2016, 2020, 2021; Menni *et al.*, 2010; García *et al.*, 2010). The relative influence of temperature is higher within marine environment, where the spatial-temporal variability affects the distribution (Cortés *et al.*, 2011a, b; Jaureguizar *et al.*, 2020), reproductive pattern (Colonello *et al.*, 2014; Elisio *et al.*, 2017), and large-scale horizontal movements (Jaureguizar *et al.*, 2018; De Wysiecki *et al.*, 2020) of elasmobranchs. The poleward shift of the SACZ in recent years, associated with the poleward expansion of the South Atlantic subtropical high (Zilli *et al.*, 2019) would also force the southward displacement of warmer waters into the SWAO, which in turn would favor the occurrence of the intra-seasonal events associated with EOF1 negative phase. This could explain the higher “tropicalization” of the coastal marine community (*i.e.*, the occasional occurrence of more than 30 tropical and subtropical species) observed along the northern Argentinean coast during the last decade (Milessi *et al.*, 2018). Therefore, as a relevant predictor of fish availability along the SWACS NACS, the predictability of temperature spatial distribution is an essential instrument to develop management strategies within the climatic change scenarios going on in the South Atlantic Ocean.

Declarations

Acknowledgments. SST data were provided by the NOAA CoastWatch Program, NOAA NESDIS Office of Satellite Data Processing and Distribution, and NASA's Goddard Space Flight Center, OceanColor Web (https://coastwatch.pfeg.noaa.gov/infog/BA_ssta_las.html). Data of relevant atmospheric variables were obtained from the National Center for Environmental Prediction–National Center for Atmospheric Research (NCEP–NCAR) reanalysis dataset (Kalnay *et al.*, 1996) through the IRI Data Library and from the ERA Interim reanalysis from the European Centre for Medium-Range Weather Forecasts (Dee *et al.*, 2011). Outgoing Longwave Radiation (OLR) data, considered as a proxy of atmospheric convection, were obtained from the National Oceanic and Atmospheric Administration (NOAA) gridded dataset. This work is a contribution to the ANPCyT (National Agency for Scientific and Technological Research of Argentina) 2015-1934 and the UBACYT (Secretariat of Science and Technology – University of Buenos Aires) 20020190100200BA Projects. Dr. Luz Clara, Dr. Vera, Dr. Alvarez and Dr. Simionato's salaries were paid by

the CONICET (National Council of Scientific and Technical Research of Argentina). Dr. Jaureguizar's salary was paid by the Scientific Research Commission (CIC) of Buenos Aires Province. INIDEP (National Institute for Fisheries Research and Development) contribution #.....

- **Fundings.** This research was supported by the ANPCyT 2015-1934 and the UBACYT 20020190100200BA Projects. Dr. Luz Clara, Dr. Vera, Dr. Alvarez and Dr. Simionato's salaries were paid by the CONICET. Dr. Jaureguizar's salary was paid by the CIC-Provincia de Buenos Aires.
- **Conflicts of interest/Competing interests.** 'Not applicable'. The authors declare no conflicts of interest.
- **Availability of data and material.** The SST data that support the findings of this study are available in NOAA CoastWatch Program, NOAA NESDIS Office of Satellite Data Processing and Distribution, and NASA's Goddard Space Flight Center, OceanColor Web at https://coastwatch.pfeg.noaa.gov/infog/BA_ssta_las.html. The relevant atmospheric variables data that support the findings of this study are available in National Center for Environmental Prediction–National Center for Atmospheric Research (NCEP–NCAR) reanalysis dataset (Kalnay et al., 1996) through the IRI Data Library and from the ERA Interim reanalysis from the European Centre for Medium-Range Weather Forecasts (Dee et al., 2011) at <https://www.ecmwf.int/en/forecasts/datasets/reanalysis-datasets/era-interim>. Outgoing Longwave Radiation (OLR) data, considered as a proxy of atmospheric convection, were obtained from the National Oceanic and Atmospheric Administration (NOAA) gridded dataset at https://psl.noaa.gov/data/gridded/data.interp_OLR.html. The datasets analyzed during the current study are available from the corresponding author on reasonable request.
- **Code availability.** The code used during the current study is available from the corresponding author on reasonable request.

References

1. Alexander MA, Scott JD (1997). Surface flux variability over the North Pacific and North Atlantic Oceans. *J. Climate* 10: 2963–78.
2. Alvarez MS, Vera CS, Kiladis GN *et al.* (2016). *Clim. Dyn.* 46: 245. <https://doi.org/10.1007/s00382-015-2581-6>.
3. Alvarez, MS; Vera, CS; Kiladis, GN (2017). MJO Modulating the Activity of the Leading Mode of Intraseasonal Variability in South America. *Atmosphere* 8, 12: 232. <https://doi.org/10.3390/atmos8120232>
4. Barreiro M, Sitz L, de Mello S, Fuente Franco R, Renom M, Farneti, R (2018). Modeling the role of Atlantic air-sea interaction in the impact of MJO on South American climate. *International Journal Climatol*, 13.
5. Berbery EH, Nogués-Paegle J (1993). Intraseasonal interactions between the Tropics and extratropics in the Southern Hemisphere. *Journal of the Atmospheric Sciences*, 50, 1950–1965.

6. Carvalho LMV, Jones C, Ambrizzi T (2005). Opposite phases of the Antarctic oscillation and relationships with intraseasonal to interannual activity in the tropics during the austral summer. *Journal of Climate*, 18(5):702–718.
7. Carvalho LM, Jones C, Liebmann B (2004). The South Atlantic Convergence Zone: Intensity, Form, Persistence, and Relationships with Intraseasonal to Interannual Activity and Extreme Rainfall. *J. Climate*, 17, 88–108, [https://doi.org/10.1175/1520-0442\(2004\)017<0088:TSACZI>2.0.CO;2](https://doi.org/10.1175/1520-0442(2004)017<0088:TSACZI>2.0.CO;2).
8. Combes V, Matano RP (2018). The Patagonian shelf circulation: Drivers and variability. *Progress in Oceanography*, Volume 167, 24–43, ISSN 0079-6611, <https://doi.org/10.1016/j.pocean.2018.07.003>.
9. Cortés F, Jaureguizar AJ, Menni RC, Guerrero RA (2011a). Ontogenetic habitat preferences of the narrownose smooth-hound shark, *Mustelus schmitti*, in two Southwestern Atlantic Coastal Systems. *Hydrobiologia*, 661(1), 445–456. DOI 10.1007/s10750-010-0559-2
10. Cortés F., Jaureguizar AJ, Guerrero RA, Dogliotti A (2011b). Influence of estuarine and continental shelf water advection on the coastal movements of apron ray, *Discopyge tschudii*, in the Southwestern Atlantic. *Journal of Applied Ichthyology* 27: 1278–1285. DOI: 10.1111/j.1439-0426.2011.01821.x
11. Colonello JH, Cortés F, Massa AM (2014). Species richness and reproductive modes of chondrichthyans in relation to temperature and fishing effort in the Southwestern Atlantic Shelf (34–54°S). *Fisheries Research* 160: 8–17
12. De Wysiecki AM, Sánchez-Carnero N, Irigoyen AJ, Milessi AC, Colonello JH, Bovcon ND, Cortés F, Barbini SA, Cedrola PV, Coller NM, Jaureguizar AJ (2020). Using temporally explicit habitat suitability models to infer the migratory pattern of a large mobile shark. *Can. J. Fish. Aquat. Sci.* 77 (9): 1529–1539. <https://doi.org/10.1139/cjfas-2020-0036>
13. Dee DP, Uppala SM, Simmons AJ, Berrisford P, Poli P, Kobayashi S, Andrae U, Balmaseda MA, Balsamo G, Bauer P, Bechtold P, Beljaars AC, van de Berg L, Bidlot J, Bormann N, Delsol C, Dragani R, Fuentes M, Geer AJ, Haimberger L, Healy SB, Hersbach H, Hólm EV, Isaksen I, Kållberg P, Köhler M, Matricardi M, McNally AP, Monge-Sanz BM, Morcrette J, Park B, Peubey C, de Rosnay P, Tavolato C, Thépaut J, Vitart F (2011). The ERA-Interim reanalysis: configuration and performance of the data assimilation system. *Q.J.R. Meteorol. Soc.*, 137: 553–597. doi:10.1002/qj.828.
14. Delgado AL, Jamet C, Loisel H, Vantrepotte V, Perillo GME, Piccolo MC (2014). Evaluation of the MODIS-aqua sea-surface temperature product in the inner and mid-shelves of southwest Buenos Aires Province, Argentina. *International Journal of Remote Sensing*, 35(1), 306–320.
15. Deser C, Alexander MA, Xie S-P, Phillips AS (2010). Sea surface temperature variability: Patterns and mechanisms. *Annual Review of Marine Science*, 2 (1), pp. 115–143.
16. Duchon CE (1979). Lanczos filtering in one and two dimensions. *J Appl Meteorol* 18(8):1016–1022.
17. Elisio M, Colonello JH, Cortés F, Jaureguizar AJ, Somoza GM, Macchi GJ (2017). Aggregations and reproductive events of the narrownose smooth-hound shark, *Mustelus schmitti*, in relation to temperature and depth in coastal waters of the southwestern Atlantic Ocean (38–42°S). *Marine and Freshwater Research*, 68, 732–742.

18. Feldstein SB (2003). The dynamics of NAO teleconnection pattern growth and decay. *Quarterly Journal of the Royal Meteorological Society*, 129, 901–924.
19. Flatau M, Kim Y-J (2013). Interaction between the MJO and polar circulations. *Journal of Climate*, 26(11):3562–3574.
20. Framiñan MB (2005). On the physics, circulation and exchange processes of the Río de la Plata estuary and the adjacent shelf. Doctoral Dissertation, University of Miami, Rosenstiel School of Marine and Atmospheric Science, Miami, Florida, USA, 486pp.
21. García M, Jaureguizar AJ, Protogino L (2010). Fish assemblages across the marine to low salinity transition zone of Rio de la Plata estuary, South America. *Latin American Journal of Aquatic Research* 38(1), 81–96 DOI: 10.3856/vol38-issue1-fulltext-8
22. Guerrero RA, Acha EM, Framiñan MB, Lasta CA (1997). Physical oceanography of the Río de la Plata Estuary, Argentina. *Continental Shelf Research* 17 (7), 727–742.
23. Hendon HH, Salby ML (1994). The Life Cycle of the Madden–Julian Oscillation. *J. Atmos. Sci.*, 51, 2225–2237, [https://doi.org/10.1175/1520-0469\(1994\)051<2225:TLCOTM>2.0.CO;2](https://doi.org/10.1175/1520-0469(1994)051<2225:TLCOTM>2.0.CO;2)
24. Jaureguizar AJ, Menni R, Lasta C, Guerrero R (2006). Fish assemblages of the Northern Argentine Coastal System: spatial patterns and their temporal variations. *Fisheries Oceanography* 15, 4: 326–344
25. Jaureguizar AJ, Solari A, Cortés F, Milessi AC, Militelli MI, Camiolo MD, Luz Clara M, García M (2016). Fish diversity in the Río de la Plata and adjacent waters: an overview on the environment influence on its spatial and temporal structure. *Journal of Fish Biology*, 89, 569–600.
26. Jaureguizar AJ, Argemi F, Trobbiani G, Palam ED, Irigoyen AJ (2018). Large-scale migration of a school shark, *Galeorhinus galeus*, in the Southwestern Atlantic. *Neotropical Ichthyology*, 16(1): e170050, DOI: 10.1590/1982-0224-20170050.
27. Jaureguizar AJ, De Wysiecki A, Camiolo MD (2020). Environmental influence on the inter-annual demographic variation of the narrownose smooth-hound shark (*Mustelus schmitti*, Springer 1939) in the Northern Argentine Coastal System (El Rincón, 38–42°S), *Marine Biology Research*, 16:8–9, 600–615, <https://doi.org/10.1080/17451000.2020.1868522>
28. Jaureguizar AJ, De Wysiecki A, Camiolo MD, Luz Clara M (2021). Inter-annual fluctuation in the population structure of an estuarine fish: influence of environmental drivers. *Journal of Marine Systems* 218,103526 <https://doi.org/10.1016/j.jmarsys.2021.103526>
29. Kalnay E, Kanamitsu M, Kistler R, Collins W, Deaven D, Gandin L, Iredell M, Saha S, White G, Woollen J, *et al.* (1996). The NCEP/NCAR 40-Year Reanalysis Project. *Bull. Am. Meteorol. Soc.*, 77, 437–471.
30. Kara AB, Wallcraft AJ, Hulburt HE, Loh W-Y (2009). Quantifying SST errors from an OGCM in relation to atmospheric forcing variables. *Ocean Modelling*, Volume 29, Issue 1, Pages 43–57. <https://doi.org/10.1016/j.ocemod.2009.03.001>
31. Lago LS, Saraceno M, Piola AR, Ruiz-Etcheverry LA (2021). Volume Transport Variability on the Northern Argentine Continental Shelf From In Situ and Satellite Altimetry Data. *Journal of Geophysical Research: Oceans*, 126(2). <https://doi.org/10.1029/2020JC016813>

32. Lentini CAD, Campos EJD, Podestá GP (2000). The annual cycle of satellite derived sea surface temperature on the western South Atlantic shelf *Brazilian Journal of Oceanography*, 48 (2), pp. 93–105.
33. Lercari D, Milessi AC, Vögler R, Velasco G, Jaureguizar AJ (2019). Modelos tróficos en el Atlántico Sud Occidental: evaluando la estructura y funcionamiento de ecosistemas costeros. Ch. 2.3. In: Muniz, P, Conde D, Venturini N, Brugnoli E (eds.) “Ciencias Marino Costeras en el Umbral del Siglo XXI: Desafíos en Latinoamérica y el Caribe”. Section 2. Ecología, manejo y gestión de recursos marino-costeros; 315–345 pp. AGT Editor, S. A., México. ISBN 978-607-7551-45-4.
34. Liebmann B, Smith CA (1996). Description of a Complete (Interpolated) outgoing longwave radiation dataset. *Bull. Am. Meteorol. Soc.*, 77, 1275–1277.
35. Luz Clara M, Simionato CG, Jaureguizar AJ (2019). Annual Variability of Sea Surface Temperature in the Northern Argentinean Continental Shelf. *Geoacta*. ISSN 1852–7744. Vol 43. In press.
36. Manta G, de Mello S, Trinchin R, Badagian J, Barreiro M (2018). The 2017 record marine heat wave in the southwestern Atlantic shelf *Geophys. Res. Lett.*
37. Menni RC, Jaureguizar AJ, Stehmann MFW, Lucifora LO (2010). Marine biodiversity at the community level: zoogeography of sharks, skates, rays and chimaeras in the southwestern Atlantic. *Biodiversity and Conservation* 19, 775–796 DOI 10.1007/s10531-009-9734-z
38. Madden RA, Julian PR (1972). Description of Global-Scale Circulation Cells in the Tropics with a 40–50 Day Period. *J. Atmos. Sci.*, 29, 1109–1123, [https://doi.org/10.1175/1520-0469\(1972\)029<1109:DOGSCC>2.0.CO;2](https://doi.org/10.1175/1520-0469(1972)029<1109:DOGSCC>2.0.CO;2)
39. Milessi AC, Bruno I, Cozzolino E, Allega L, Jaureguizar AJ (2018). Cambio climático global frente a las costas de Mar del Plata: ¿evidencias de tropicalización? Informe de Investigación INIDEP N° 131, 11 pp.
40. Mukarami T, Sumi A (1981). Large-scale aspects of the 1978-79 winter circulation over the greater MONEX region. Part II: Long-period perturbations. *Journal of the Meteorological Society of Japan*, 59, 646–671.
41. Paegle JN, Mo KC (2002). Linkages between summer rainfall variability over South America and sea surface temperature anomalies. *Journal of Climate*, 15 (12), pp. 1389–1407.
42. Pimenta F, Garvine RW, Munchow A (2008). Observations of coastal upwelling off Uruguay downshelf of the Plata estuary, South America. *Journal of Marine Research*, Vol. 66, No. 6., pp. 835–872.
43. Podestá GP, Brown OB, Evans RH (1991). The annual cycle of satellite-derived sea surface temperature in the Southwestern Atlantic Ocean *J. Climate*, 4(4):457–467.
44. Pohl B, Fauchereau N, Reason CJC, Rouault M (2010). Relationships between the Antarctic Oscillation, the Madden–Julian Oscillation, and ENSO, and consequences for rainfall analysis. *Journal of Climate*, 23(2):238–254.
45. Powell BS, Arango HG, Moore AM, Di Lorenzo E, Milliff RF, Foley D (2008). 4D VAR data assimilation in the Intra-Americas Sea with the Regional Ocean Modeling System (ROMS). *Ocean Modelling*, 25,

173–1884.

46. Reynolds RW, Rayner NA, Smith TM, Stokes DC, Wang W (2002). An improved in situ and satellite SST analysis for climate. *Journal of Climate*, 15, 1609–1625.
47. Rivas AL (2010). Spatial and temporal variability of satellite-derived sea surface temperature in the southwestern Atlantic Ocean, *Continental Shelf Research*, 30, 7, pp 752–760, ISSN 0278–4343, <https://doi.org/10.1016/j.csr.2010.01.009>.
48. Rodrigues Chaves RR, Nobre PJL (2004). Interactions between sea surface temperature over the South Atlantic Ocean and the South Atlantic Convergence Zone. *Geophysical Research Letters*. doi:10.1029/2003GL018647.
49. Rodrigues RR, Taschetto AS, Sen Gupta A, Foltz, GR (2019). Common cause for severe droughts in South America and marine heatwaves in the South Atlantic. *Nature Geosciences* 12.
50. Rodrigues RR, Woollings T (2017). Impact of atmospheric blocking on South America in austral summer. *Journal of Climate*, 30(5).
51. Saraceno M, Simionato CG, Ruiz-Etcheverry LA (2014). Sea surface height trend and variability at seasonal and interannual time scales in the South eastern South American continental shelf between 27°S and 40°S, *Continental Shelf Research*, 91, 82–94.
52. Scasso L, Piola A (1988). Intercambio neto de agua entre el mar y la atmósfera en el Golfo San Matías. *Oceanologica Acta*, 15(1): 13–31.
53. Simionato CG, Meccia VL, Dragani WC, Guerrero RA, Nuñez MN (2006). The Río de la Plata estuary response to wind variability in synoptic to intraseasonal scales: Barotropic response. *J. Geophys. Res.* 111 (C09031).
54. Simionato CG, Meccia VL, Guerrero RA, Dragani WC, Nuñez MN (2007). Río de la Plata estuary response to wind variability in synoptic to intraseasonal scales: 2. Currents' vertical structure and its implications for the salt wedge structure. *J. Geophys. Res.* 112, C07005. <http://dx.doi.org/10.1029/2006JC003815>.
55. Simionato CG, Luz Clara Tejedor M, Campetella C, Guerrero R, Moreira D (2010). Patterns of Sea Surface Temperature Variability on seasonal to subannual scales at and offshore the Río de la Plata Estuary. *Continental Shelf Research*, 30, 1983–1997.
56. Stan C, Straus DM, Frederiksen JS, Lin H, Maloney ED, Schumacher C (2017). Review of tropical-extratropical teleconnections on intraseasonal time scales. *Reviews of Geophysics*, 55, 902–937. <https://doi.org/10.1002/2016RG000538>.
57. Sterl A, Hazeleger W (2003). Coupled variability and air-sea interaction in the South Atlantic Ocean, *Clim. Dyn.*, 21, 559–571, doi:10.1007/s00382-003-0348-y.
58. Tirabassi G, Masoller C, Barreiro M (2014). A study of the air-sea interaction in the South Atlantic Convergence Zone through Granger Causality Int. *J. Climatology*.
59. Trinchin R, Ortega L, Barreiro M (2019). Spatio-temporal characterization of summer coastal upwelling events in Uruguay, South America. *Reg. Studies in Marine Sci.* 31.

60. Venegas SA, Mysak LA, Straub DN (1997). Atmosphere-ocean coupled variability in the South Atlantic. *Journal of Climate*, v. 10, n. 11, pp. 2904–2920.
61. Vera CS, Alvarez MS, Gonzalez PLM, Kiladis GN, Liebmann B (2017). Seasonal cycle of precipitation variability in South America on intraseasonal timescales. *Climate Dynamics*. In press (published on-line <https://doi.org/10.1007/s00382-017-3994-1>).
62. Wang J, Wen Z, Wu R, Guo Y, Chen Z (2016). The mechanism of growth of the low-frequency East Asia-Pacific teleconnection and the triggering role of tropical intra-seasonal oscillation. *Climate Dynamics*, 46, 3965–3977. <https://doi.org/10.1007/s00382-015-2815-7>.
63. Zhang C (2005). Madden-Julian Oscillation, *Rev. Geophys.*, 43, RG2003, doi:10.1029/2004RG000158.
64. Zilli MT, Carvalho LMV, Lintner BR (2019). The poleward shift of South Atlantic Convergence Zone in recent decades. *Clim Dyn* 52, 2545–2563. <https://doi.org/10.1007/s00382-018-4277-1>

Figures

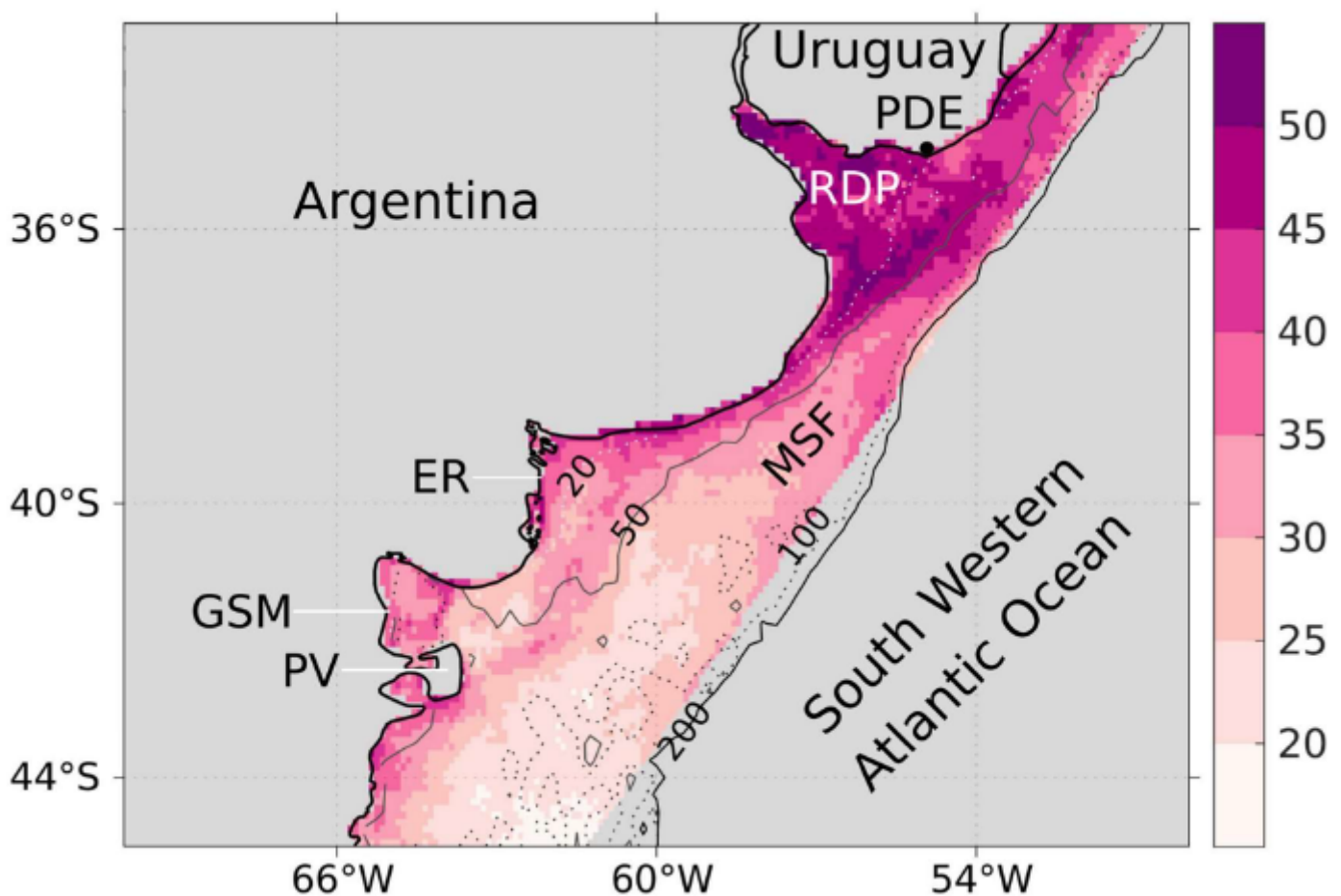


Figure 1

Southwestern Atlantic Continental Shelf (study area) showing isobaths and the principal geographical references: Río de la Plata (RDP), El Rincón (ER), San Matias Gulf (GSM), Península Valdés (PV) and Punta del Este (PDE). Shading indicates the percentage of SST variability explained by the intraseasonal time scale.

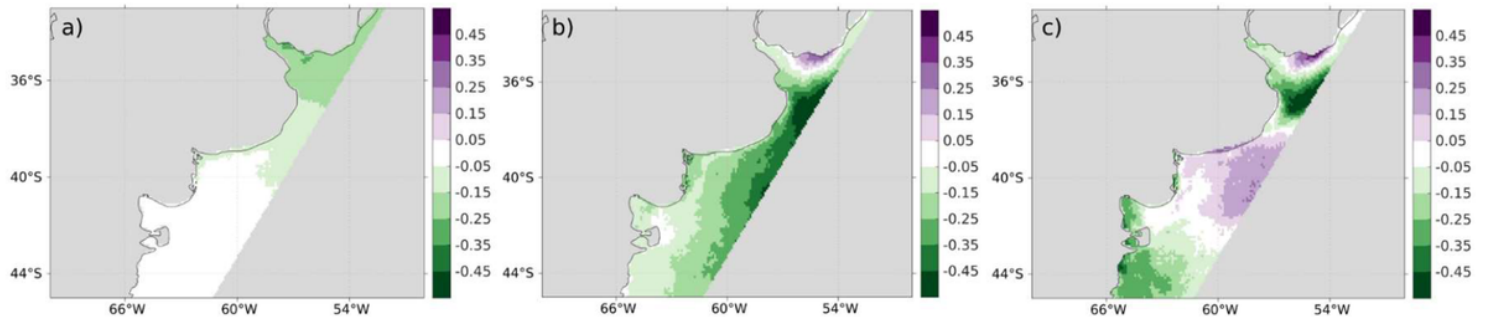


Figure 2

STA variability patterns (EOF spatial structure) associated with (a) EOF1, explaining 25.7% of total variance; (b) EOF2, 9.0%; and (c) EOF3, 5.1%.

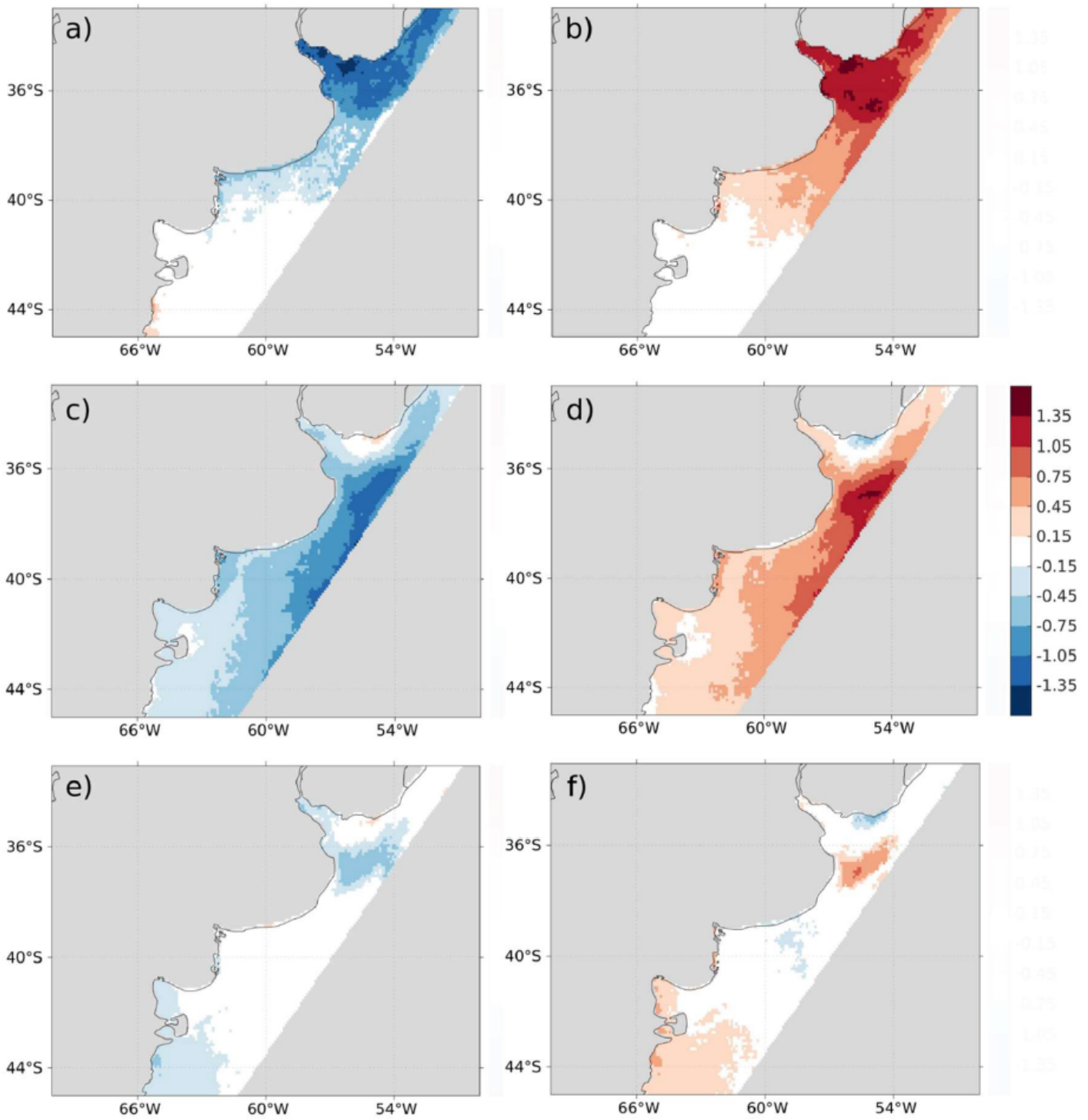


Figure 3

Composites of the blended SSTA ($^{\circ}\text{C}$) fields for the Southwestern Atlantic Continental Shelf associated with the EOF1 (upper panels), the EOF2 (middle panels) and the EOF3 (lower panels) of IS variability in its positive (a., c. and e.) and negative (b., d. and f.) phases. Coloured areas indicate significance to the 95 % confidence level.

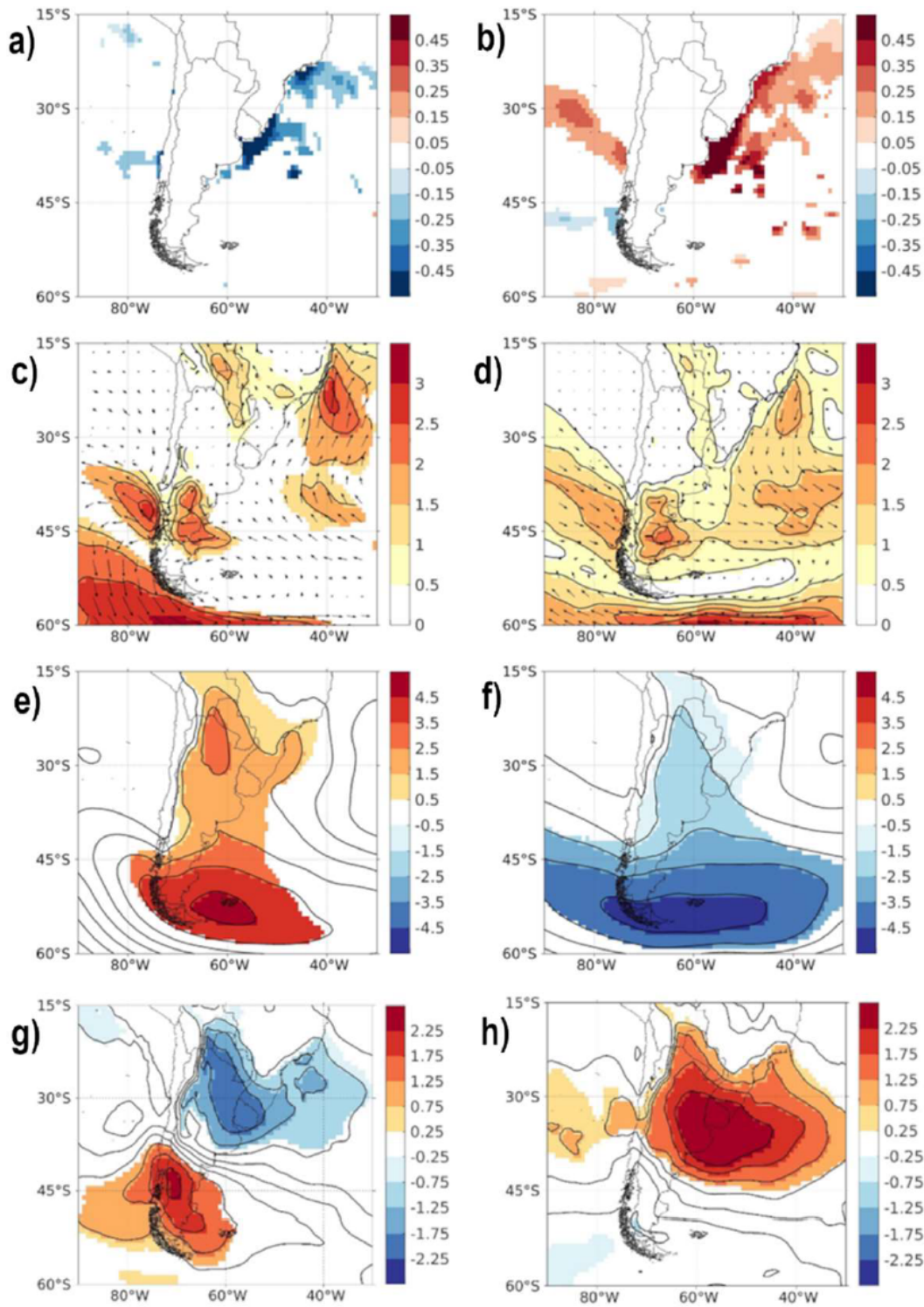


Figure 4

Composite maps of ERA-interim 10-90-day filtered anomalies of: SST ($^{\circ}\text{C}$, a and b), zonal and meridional wind at 10 meters (vectors) and its magnitude (colors, in ms^{-1} , c and d), SLP (mb, e and f), and 925 hPa air temperature ($^{\circ}\text{C}$, g and h) for EOF1 positive events (left) and negative events (right). Shading indicates statistically significant regions at 95% (see text for details)

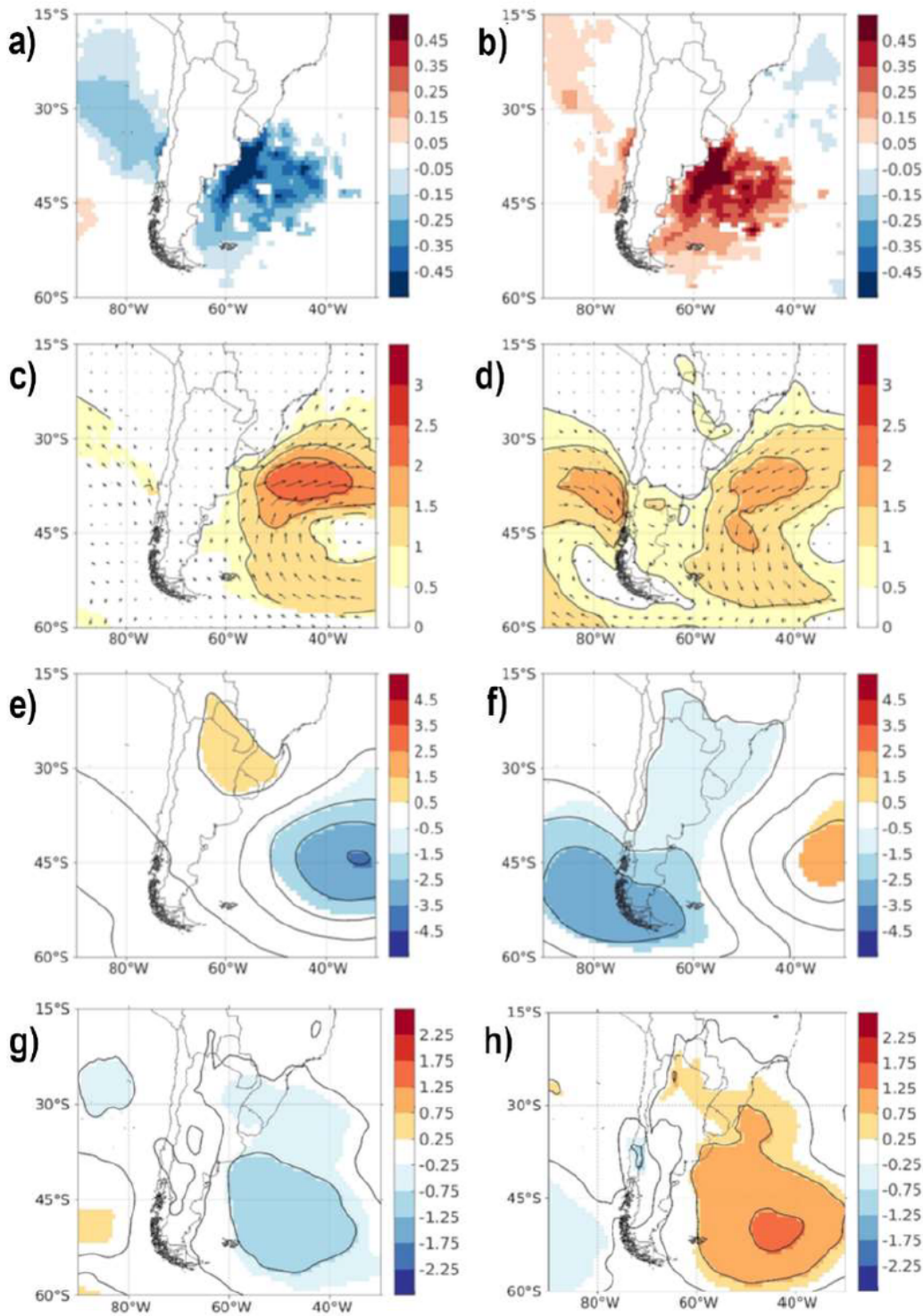


Figure 5

Composite maps of ERA-interim 10-90-day filtered anomalies of: SST ($^{\circ}\text{C}$, a and b), zonal and meridional wind at 10 meters (vectors) and its magnitude (colors, in ms^{-1} , c and d), SLP (mb, e and f), and 925 hPa air temperature ($^{\circ}\text{C}$, g and h) for EOF2 positive events (left) and negative events (right). Shading indicates statistically significant regions at 95% (see text for details)

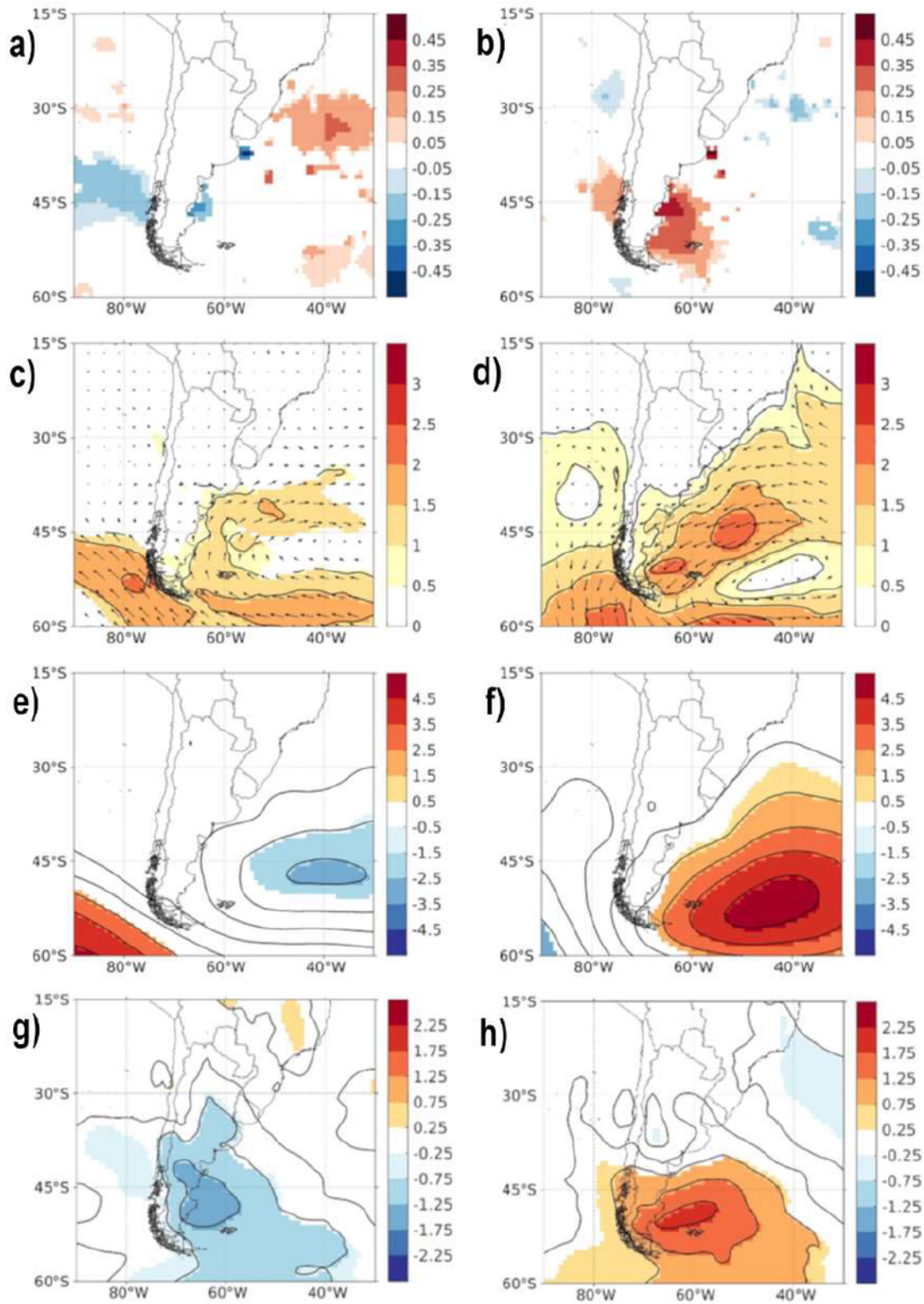


Figure 6

Composite maps of ERA-interim 10-90-day filtered anomalies of: SST ($^{\circ}\text{C}$, a and b), zonal and meridional wind at 10 meters (vectors) and its magnitude (colors, in ms^{-1} , c and d), SLP (mb, e and f), and 925 hPa air temperature ($^{\circ}\text{C}$, g and h) for EOF3 positive events (left) and negative events (right). Shading indicates statistically significant regions at 95% (see text for details)

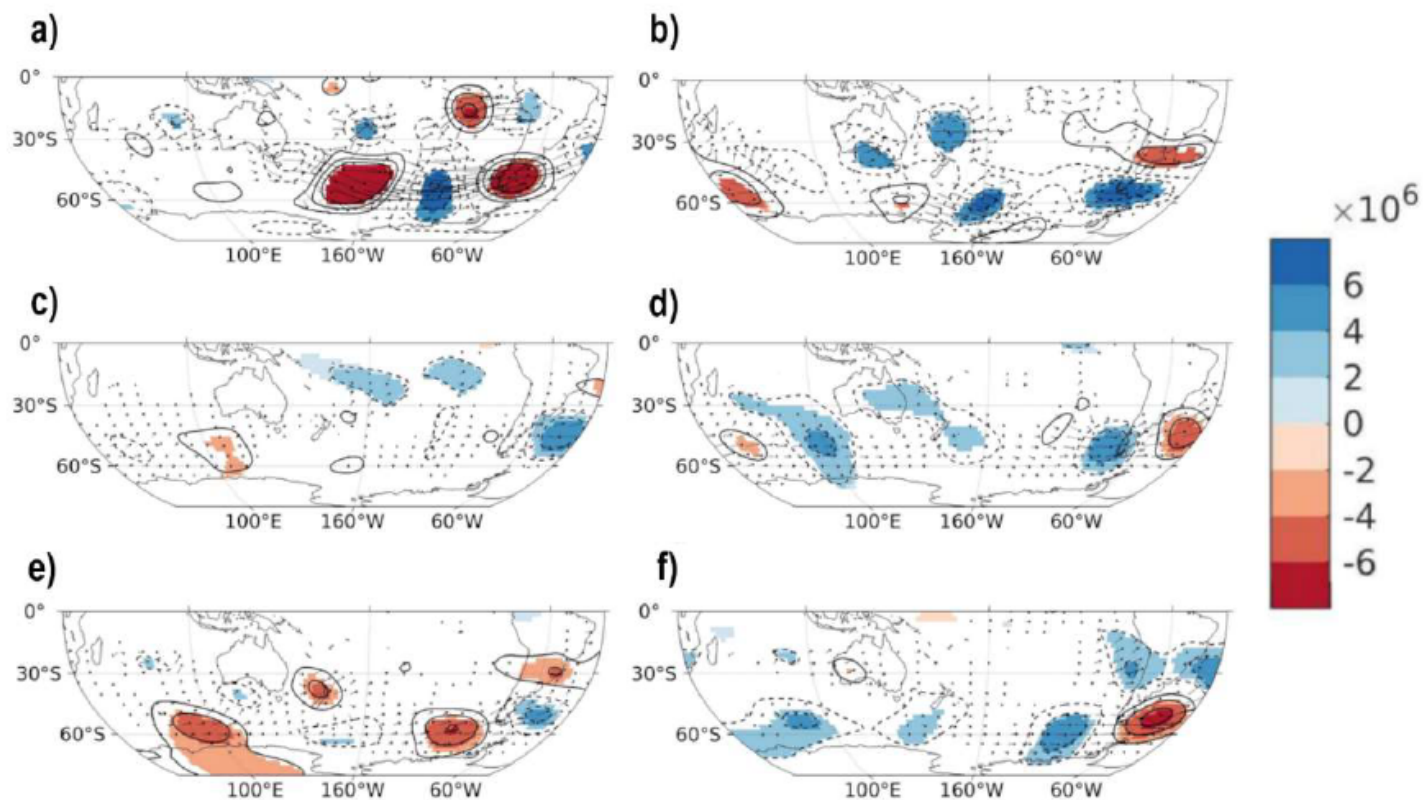


Figure 7

Composite maps of 10-90 day filtered anomalies of daily stream function at 250 mb ($m-2s^{-1}$, contours, shading) and derived wave activity fluxes (vectors) for positive events (left) and negative events (right) of EOF1 (a and b), EOF2 (c and d) and EOF3 (e and f). Negative contours are dashed and 0 contour is omitted. Coloured areas indicate significance to the 95 % confidence level

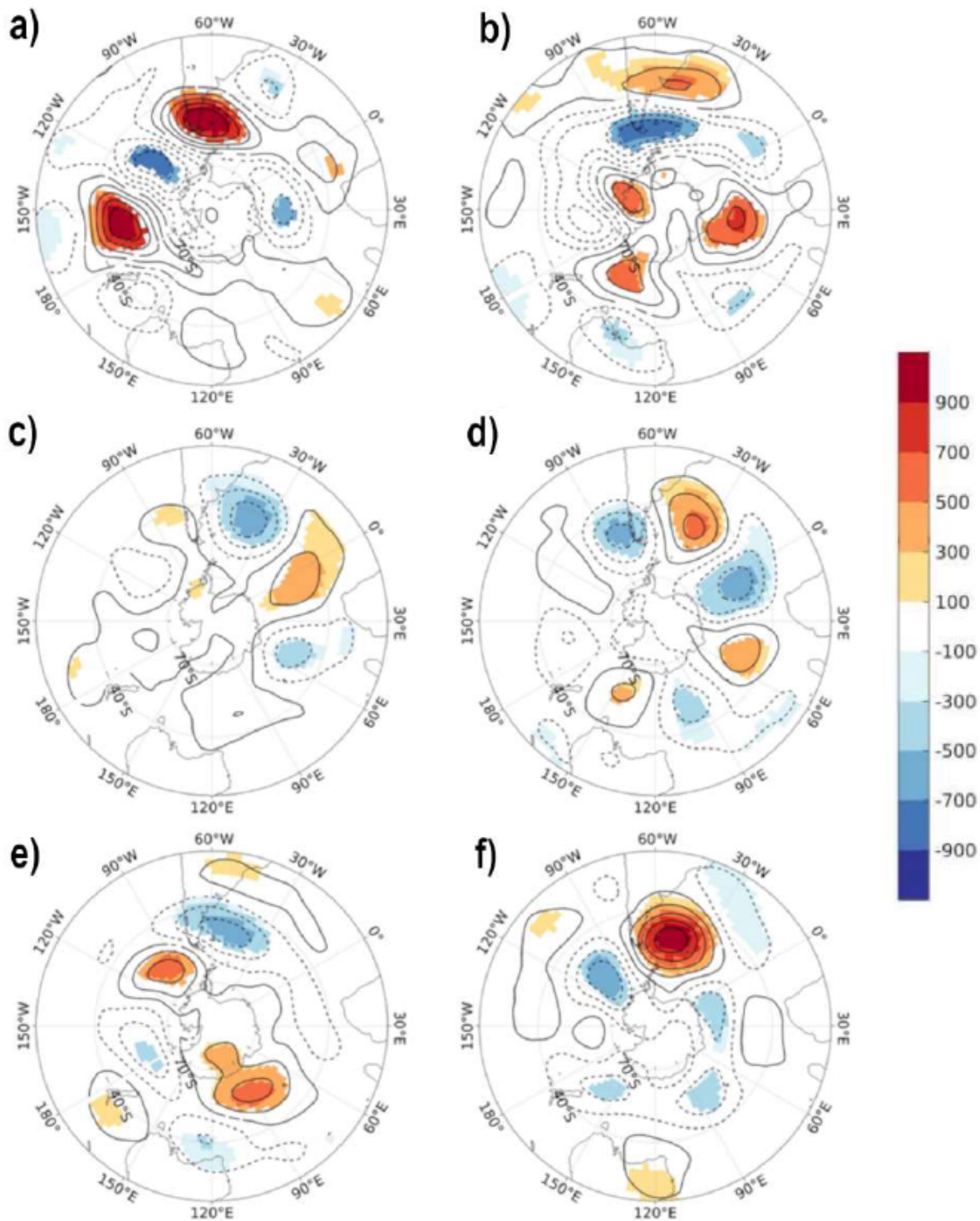


Figure 8

Composite maps of 10-90 day filtered anomalies of 300 mb geopotential heights presented in stereographic projection. Negative contours are dashed and 0 contour is omitted. Coloured areas indicate significance to the 95 % confidence level. a) EOF1 positive, b) EOF1 negative, c) EOF2 positive, d) EOF2 negative, e) EOF3 positive, and f) EOF3 negative

Supplementary Files

This is a list of supplementary files associated with this preprint. Click to download.

- [SuppFig1.pdf](#)